

Understanding tungsten accumulation during ICRH operation on WEST

P Maget, P Manas, R Dumont, C Angioni, J-F Artaud, C Bourdelle, L Colas, P Devynck, D Fajardo, N Fedorczak, et al.

▶ **To cite this version:**

P Maget, P Manas, R Dumont, C Angioni, J-F Artaud, et al.. Understanding tungsten accumulation during ICRH operation on WEST. 48TH Conference on Plasma Physics, EPS, Jun 2022, Virtual event, Netherlands. cea-03740593

HAL Id: cea-03740593
https://cea.hal.science/cea-03740593

Submitted on 29 Jul 2022

HAL is a multi-disciplinary open access archive for the deposit and dissemination of scientific research documents, whether they are published or not. The documents may come from teaching and research institutions in France or abroad, or from public or private research centers.

L'archive ouverte pluridisciplinaire **HAL**, est destinée au dépôt et à la diffusion de documents scientifiques de niveau recherche, publiés ou non, émanant des établissements d'enseignement et de recherche français ou étrangers, des laboratoires publics ou privés.

Understanding tungsten accumulation during ICRH operation on WEST

P. Maget, P. Manas, R. Dumont, C. Angioni[1], J-F Artaud, C. Bourdelle, L. Colas,
P. Devynck, D. Fajardo[1], N. Fedorczak, M. Goniche, J. Hillairet, Ph. Huynh,
J. Morales, V. Ostuni, D. Vézinet and the WEST team*

CEA, IRFM, F-13108 Saint Paul-lez-Durance, France. [1] *Max-Planck-Institut für Plasmaphysik, D-85748 Garching, Germany.* * *see http://west.cea.fr/WESTteam*

Summary The transport of impurities in a tokamak with metallic walls can lead to accumulation events and radiative collapses, and this is particularly true when neoclassical transport is enhanced by sources of impurity poloidal asymmetry [1, 2]. On WEST, where the RF heating scheme (torque-free without core particle sources) is relevant for ITER operation, these events are rare, but still radiative collapses are sometimes observed [3, 4]. The physics of collisional tungsten transport in this case involves 3 main channels: i) a direct channel by which the hydrogen temperature anisotropy driven by ICRH drives a poloidal asymmetry of the electrostatic potential, ii) a non-linear channel by which the tungsten accumulation mitigates the ICRH drive by increasing the parallel temperature of the fast ions and reducing the temperature anisotropy in a self-limited process, and iii) an indirect channel related with the ICRH induced toroidal rotation. The role of Finite Orbit Width (FOW) effects is found to be instrumental : it strongly reduces the hydrogen temperature anisotropy, the favorable Hydrogen Temperature Screening (HTS) effect, and the electron heat source. The tungsten peaking as a function of toroidal rotation and ICRH power shows 2 possible branches consistent with bolometry inversion, one with a peaking driven by ICRH and one with a peaking driven by rotation. The condition for a radiative collapse in the core brings an additional constraint, and indicates that the electron heat source is probably much lower than computed, suggesting important losses of fast ions in the ripple. The radiative collapse would then be due to a limited electron heat source and a tungsten peaking driven by the induced rotation. This peaking is initially moderate, and it is reinforced during the collapse as the temperature screening effect reverses.

Observation of a radiative collapse during ICRH operation, and modelling tools An example of radiative collapse during ICRH operation is shown in fig. 1. The plasma current is 0.5 MA and the magnetic field 3.7 T in this experiment, operated in L-mode at a Greenwald fraction around 60%. As the power is ramped up, the radiative power in the core region slowly increases and as the power exceeds 4.3 MW the collapse takes place. The tungsten peaking $n_W(0)/n_W(0.3)$ reconstructed by bolometry inversion shows a moderate value around 1.5 before the collapse, but it rapidly increases to about 4 during the fall of the core temperature. Although we have no core rotation measurement for this experiment, the acceleration of a magnetic island located near the plasma edge at $q = 4$ shows that plasma rotation is modified by ICRH. We

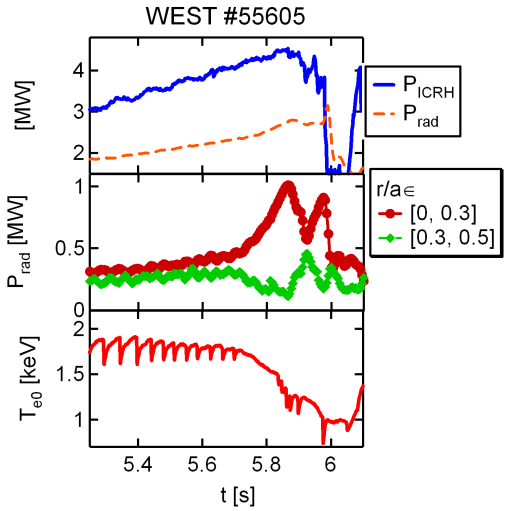


Figure 1: *Radiative collapse in ICRH operation: ICRH and radiative power, radiative losses in central and peripheral regions, and core electron temperature.*

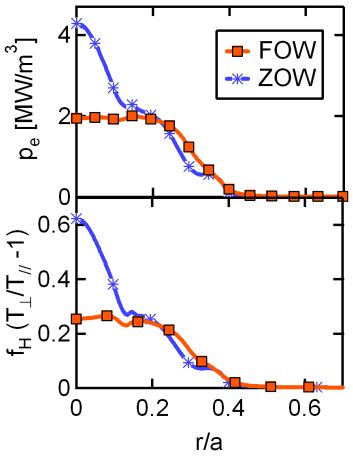


Figure 2: *Electron heat source (top) and normalized temperature anisotropy (bottom) with / without FOW effects (EVE/AQL).*

analyze here this experiment with the collisional transport codes FACIT [5, 6] and NEO [7], the suite of codes EVE [8] and AQL [9] for the ICRH heat deposition and temperature anisotropy, and the METIS integrated simulation tool for the current profile evolution [10].

ICRH deposition : Finite Orbit Width (FOW) effects The hydrogen temperature anisotropy that forms the main specific drive for tungsten peaking during ICRH is very sensitive to Finite Orbit Width (FOW) effects as the perpendicular temperature becomes large. A surrogate model for FOW effects has been implemented in EVE, correcting the Zero Orbit Width (ZOW) computation. We find that both the electron power density and the temperature anisotropy are strongly reduced in the core region (fig. 2), thus reducing at the same time the margins for compensating core radiation and the drive for tungsten peaking through the electrostatic force. Another consequence is that the Hydrogen Temperature Screening effect, that produces an outward tungsten pinch for a sufficiently large radial gradient of the perpendicular hydrogen temperature [11], is strongly reduced in the core. This is verified with NEO [7]: when FOW effects are neglected, a hollow tungsten profile is expected (fig. 3), in contradiction with experimental observations.

Tungsten peaking: the 3 channels There are 3 main channels by which the tungsten profile in the plasma core is influenced by ICRH. The first one is direct, and is due to the poloidal asymmetry of the electrostatic potential. It generates an increased W concentration at the High Field Side, which is higher with the temperature anisotropy of the hydrogen minority. The second one is non-linear and has not been considered in previous studies. It is related with the increase

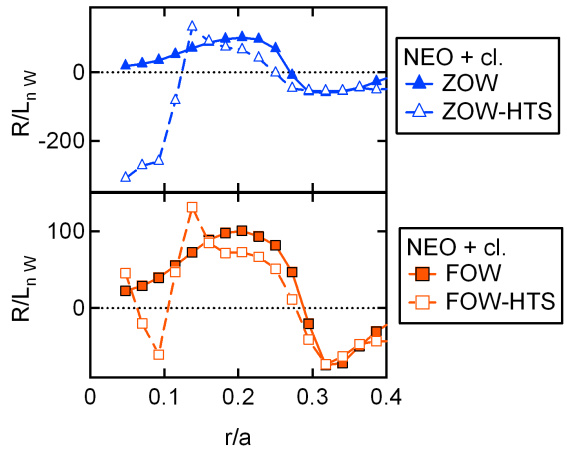


Figure 3: *Normalized tungsten gradient computed with NEO without (top) and with (bottom) FOW effects, and with / without HTS effect.*

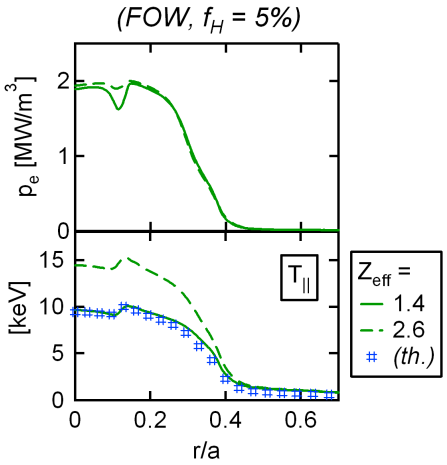


Figure 4: *Electron heat source (top) and parallel hydrogen temperature (bottom) computed by EVE/AQL for* $Z_{eff} = 1.4$ *and* 2.6*, and theory* $T_{\|} \propto Z_{eff}^{2/3}$ *("th.").*

of the parallel hydrogen temperature by pitch angle scattering on impurities [12], and gives $T_{\|} \propto Z_{eff}^{2/3}$, while the perpendicular temperature and electron heat source remain unchanged, as verified with EVE/AQL (fig. 4). The accumulation of tungsten in the core tends therefore to reduce the temperature anisotropy $T_{\perp}/T_{\|}$ (direct channel), and leads to a self-regulating mechanism. Finally, the third channel is indirect, and is related with the ICRH induced rotation.

The steady-state tunsgten profile in the core is determined using the collisional transport code FACIT [5, 6], and a map of the tungsten peaking as a function of toroidal rotation and ICRH power is computed using EVE/AQL results at $t = 5.6s$, just before the radiative collapse, with a temperature anisotropy assumed to be proportional to the ICRH power (fig. 5). This diagram shows two regions of large tungsten peaking : one at low rotation where the peaking is due to ICRH (direct channel), and one at large rotation where it is due to the centrifugal force (indirect channel in the absence of external torque). The two regions are separated by a valley where the tungsten profile is nearly flat.

Understanding the collapse The experimental situation can be evaluated by using the inverted bolometry signals, that give at $t = 5.6s$ a power radiated inside $r/a = 0.3$ of about 0.4 MW. Mapping this constraint in the diagram of figure 5 gives 2 branches of solutions, on both sides of the valley (stars in the bottom plot of fig. 5). If we add the criterion p_e/p_{rad}^{max} that should approach unity at the time when the collapse starts, we find that the low rotation branch is disqualified, with a ratio that is below 40%. The collapse criterion can be met only on the larger rotation branch, but then the effective ICRH power should be significantly lower than computed.

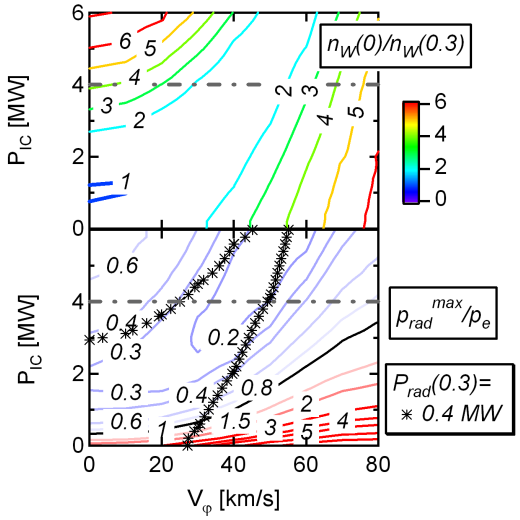


Figure 5: *Tungsten peaking and ratio p_{rad}^{max}/p_e as a function of toroidal rotation and ICRH power.*

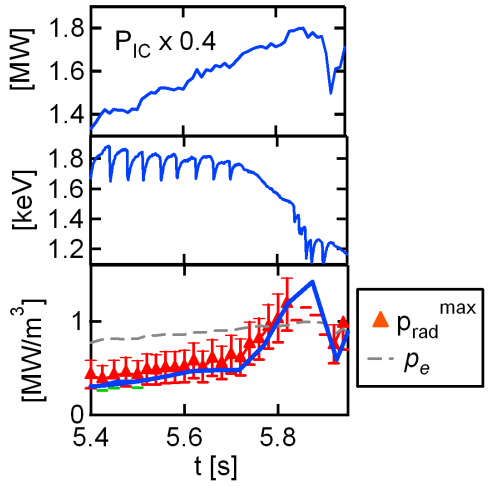


Figure 6: *ICRH power (reduced by 60%), core electron temperature, predicted and bolometry inverted maximum radiated power density, and electron heat source (p_e).*

In such case, the linear relation that has been assumed between the electron heat source and the temperature anisotropy is no longer valid, and the analysis can only provide a rough estimate of the real situation. If we reduce the ICRH electron heat source and temperature anisotropy by 60%, we do cross the collapse criterion at the right time, for a plasma rotating at about 50 km/s (fig. 6). The tungsten peaking is then driven by the induced rotation, and rises strongly during the collapse as the temperature screening effect reverses.

Aknowledgments This work has been carried out within the framework of the EUROfusion Consortium, funded by the European Union via the Euratom Research and Training Programme (Grant Agreement No 101052200 - EUROfusion). Views and opinions expressed are however those of the author(s) only and do not necessarily reflect those of the European Union or the European Commission. Neither the European Union nor the European Commission can be held responsible for them.

References

[1] C. Angioni and P. Helander, Plasma Physics and Controlled Fusion 56 (2014) 124001.
[2] C. Angioni, Plasma Physics and Controlled Fusion 63 (2021) 073001.
[3] M. Goniche, submitted to Nuclear Fusion (2022).
[4] V. Ostuni, This conference O4.62 (2022).
[5] P. Maget et al., Plasma Physics and Controlled Fusion 62 (2020) 105001.
[6] D. Farajo et al., Plasma Physics and Controlled Fusion 64 (2022) 055017 .
[7] E.A. Belli and J. Candy, Plasma Physics and Controlled Fusion 50 (2008) 095010.
[8] R. Dumont, Nuclear Fusion 49 (2009) 075033.
[9] R. Dumont and D. Zarzoso, Nuclear Fusion 53 (2012) 013002.
[10] J. Artaud et al., Nuclear Fusion 58 (2018) 105001.
[11] F. Casson et al., Nuclear Fusion 60 (2020) 066029.
[12] T. Stix, Nuclear Fusion 15 (1975) 737.